THE JOURNAL OF PHYSICAL CHEMISTRY C
A JOURNAL OF THE AMERICAN CHEMICAL SOCIETY

pubs.acs.org/JPCC

Article

Structure and Electronic Effects from Mn and Nb Co-doping for Low Band Gap $BaTiO_3$ Ferroelectrics

Published as part of The Journal of Physical Chemistry virtual special issue "D. D. Sarma Festschrift".

Soham Mukherjee,* Dibya Phuyal, Carlo U. Segre, Shyamashis Das, Olof Karis, Tomas Edvinsson, and Håkan Rensmo*

Cite This: *J. Phys. Chem. C* 2021, 125, 14910−14923

Read Online

ACCESS | Metrics & More | Article Recommendations | Supporting Information

ABSTRACT: We have investigated the doping-induced local structural and electronic effects in the recently developed low band gap room temperature ferroelectric Mn−Nb co-doped $BaTiO_3$. Experimental and theoretical Raman spectroscopies are utilized to quantify the Ti off-centering, identified to be the intrinsic origin of ferroelectricity in these systems. Mn and Nb exhibit contrasting doping behaviors that have remarkable effects on $BaTiO_3$ functionality. Jahn−Teller distorted Mn^{3+} is primarily associated with lowering of the bulk band gap, while charge-compensating Nb^{5+} off-centers within the O_6 octahedra, creating a polar mode that stabilizes the ferroelectric ground state. The charge neutral aliovalent Mn^{3+}−Nb^{5+} pair effectively couples to the inherent ferroelectric instability of the $BaTiO_3$ lattice, restoring some spontaneous polarization lost by doping Mn^{3+} (d^4) ions at Ti^{4+} (d^0) sites.

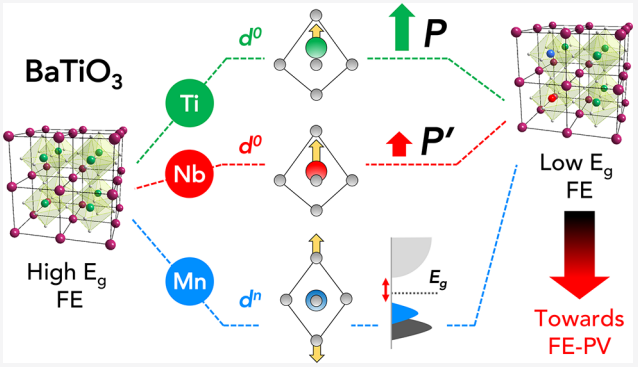

INTRODUCTION

Research on ferroelectric materials has come a long way since the discovery of the perovskite oxide $BaTiO_3$ as a ferroelectric in 1946,[1] finding a wide array of applications[2,3] in the modern age such as capacitors,[4,5] actuators,[6] sensors,[7,8] waveguide modulators,[9,10] and ferroelectric memories.[11] Ferroelectrics typically exhibit high dielectric constants and carry spontaneous lattice polarization (P) that can be reversed by using an external electric field greater than the coercive field. This intrinsic polarization can be utilized to sustain efficient separation of photogenerated electron−hole pairs, thereby generating a steady-state photocurrent. The high electric field in ferroelectrics is capable of producing above band gap voltages,[12] with controllable voltage output.[13] This fundamental advantage over conventional p−n junctions explains the tremendous interest in ferroelectric photovoltaics.[14−17]

In the classical ferroelectric $BaTiO_3$, the lowest unoccupied energy states (3d) of d^0 ion Ti^{4+} strongly hybridize with O 2p states, thus largely driving the ferroelectric distortion.[18] The Ti^{4+} ion off-centers from its centrosymmetric position in the unit cell, resulting in large inherent polarization (P = 24.1 $\mu C/cm^2$). In addition to such a high P value, $BaTiO_3$ exhibits a rich structural phase diagram, high chemical stability, and wide doping tunability of the perovskite structure ABO_3 which provides an ideal framework for tuning and exploring multifunctionalities.[19−22] However, the biggest challenge in realizing $BaTiO_3$ ferroelectrics as photovoltaics stems from its typically large bulk band gap (3.2 eV) which limits its access mostly to the UV range, as commonly observed[23,24] for all d^0-ferroelectric perovskites (e.g., $KNbO_3$ and $BaZrO_3$). This is primarily due to the requirement of partial d-occupancy on the B-site cation to reduce the optical band gap that tends to remove the ferroelectric distortion, eventually stabilizing the prototypical high-symmetry phase.[25−27] Work on improving overall performance focuses mainly on narrowing the band gap through modification in compositions and the connection between polar order and photovoltaic effect.[15] Band gap engineering via chemical substitution such as A-site La-doped $BiFeO_3$[15] and B-site Cr-doped in $BiFeO_3$ has shown remarkable overall efficiencies of nearly 8%.[24] Another route is to make solid solutions such as $[KNbO_3]_{1-x}[BaNi_{1/2}Nb_{1/2}O_{3-\delta}]_x$ which show a wide tunability with enhanced photovoltaic properties under visible light.[16] Furthermore, the

Received: March 21, 2021
Revised: June 15, 2021
Published: July 1, 2021

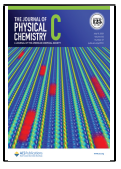

https://doi.org/10.1021/acs.jpcc.1c02539
J. Phys. Chem. C 2021, 125, 14910−14923

competing structural distortions associated with a remnant polarization are dramatically reduced as a function of doping. This complicates the trade-off between a narrow gap and large remnant polarization.

This goal was, however, recently accomplished[28] by co-doping equimolar amounts of Mn^{3+} (d^4) and Nb^{5+} (d^0) at Ti^{4+} sites in $BaTiO_3$. This doping strategy allowed for substantial band gap tunability (1.5−3.2 eV), suitable for visible light absorption, and sufficiently high P values. A P value of 1.66 eV was reported for 7.5% doping (P = 15.1 $\mu C/cm^2$), which retained ∼70% polarization of $BaTiO_3$. DFT+U calculations[28,29] revealed the doping induced midgap states to be of predominantly Mn 3d character, as was also concluded from enhancement of the Mn 3d states detected by resonant photoelectron spectroscopy,[29] identifying Jahn−Teller (JT) active Mn^{3+} (d^4) to be responsible for reduction of the observed band gap. Nb^{5+} (d^0), on the other hand, acted as a charge compensator, also capable of stabilizing ferroelectric ground states similar to ferroelectric niobates.[30−32] The Mn−Nb dopant pair dipole was argued to effectively couple to the $BaTiO_3$ lattice, thereby retaining the electric polarization to a large extent. Domain switching was observed through piezoresponse force microscopy (PFM)[33] measurements on epitaxial thin films of Mn−Nb co-doped $BaTiO_3$ (hereafter termed BTMNO) grown by pulsed later deposition, validating good ferroelectric response in films, a key step toward $BaTiO_3$-based PV[34,35] device fabrication.

While the electronic properties of the BTMNO are being investigated currently, experimental studies on the local geometric structure about the dopant ions and how they link to the electronic structure have been less explored. This is of fundamental importance, as local structural distortions operative beneath a well-defined periodic lattice[36−39] can often significantly influence material functionalities. The present work uses X-ray absorption fine structure (XAFS) with support from Raman and DFT calculations to elucidate the dopant environment: position of dopants, formal valence states, modes of distortion, and their link to the material functionality. We find Mn and Nb residing at Ti sites to be an effective charge neutral pair exhibiting fundamentally different modes of local distortions, which leads them to assume characteristic roles in the band gap engineering and retention of electrical polarization in BTMNO. The ability to control such local structures is fundamental to formulate strategies for making ferroelectric perovskites efficient solar harvesters.

METHODS

Experiments. BTMNO with x = 0.0, 0.025, 0.05, 0.075, and 0.1 were prepared by using previously reported methods.[28] Raman spectroscopy measurements were performed by using a Renishaw inVia Raman spectrometer equipped with a 633 nm wavelength laser and an edge filter for Rayleigh scattering rejection. A sharp cut of the edge filter designed for 633 nm wavelength allowed the measurements of soft modes to as low as 40 cm^{-1}.

X-ray absorption spectroscopy (XAS) measurements at the K-edges of Ti (4966 eV), Mn (6539 eV), and Nb (18986 eV) were performed at the Materials Research Collaborative Access Team (MRCAT) Sector 10 bending magnet line of the Advanced Photon Source, Argonne National Laboratory, with high photon flux (6.4×10^9 at 10 keV) and high resolution ($\Delta E/E \sim 10^{-4}$). The incident photon beam was monochromatized by using a Si (111) double-crystal monochromator detuned by 50% to remove harmonics. A mixture of N_2 and He gas was optimized to absorb ∼5−10% of the incident photons. Polycrystalline samples were first ground into a fine powder, mixed with boron nitride and PVDF, and then pressed into 7 mm diameter pellets. Samples were oriented at 45° with respect to the incident X-ray beam, thereby allowing simultaneous measurement of a reference foil using the transmitted beam intensity. Flourescence data were collected by using a four-element Vortex (Hitachi) SDD detector with xMap (XiA) digital pulse processing electronics. The step size corresponding to selected XAS energy ranges for each metal edge is provided in the Supporting Information (Table S1). The fluorescence mode data were found to be free from significant amplitude loss due to self-absorption effects. During data collection multiple scans were recorded for each sample. Comparing these individual scans against their average gives an idea about the noise level and the reliability of the data. All XAS data sets were processed and analyzed by using the Athena-Artemis software suite, a front end to FEFF and IFEFFIT.[40] The subtracted background was calculated by using the AUTOBK algorithm implemented in the software.[41]

EXAFS Analyses. The XAS data were first converted to absorption versus energy, followed by energy scale calibration, pre-edge background removal using a linear fit, and post-edge background removal using a third-order polynomial. All the spectra were normalized to have an edge step of 1. The amplitude reduction factor (S_0^2) values for Mn (0.85) and Nb (0.98) were first extracted individually and thereafter retained as constant values while performing simultaneous fits to Mn K and Nb K-edge data for all BTMNO compositions. Coordination numbers, bond distances, energy offsets, and pseudo-Debye−Waller factors (σ^2) were extracted as local structural parameters. For Ti K-edge data, strong interference with the Ba L_3 (5247 eV) edge limits usable k_{max} to ∼8.2 $Å^{-1}$, rendering EXAFS resolution too poor to account for Ti off-centering in terms of three different Ti−O bond lengths. Thus, the modulus of Fourier transforms of $\chi(k)$ over the range 2.0−8.0 $Å^{-1}$ for the Ti K-edge data (Figure 2d) has been interpreted qualitatively and compared to results obtained from the pre-edge fine structure analyses. For both dopant K-edges (Mn and Nb), longer k ranges could be extracted: 2.0−9.0 $Å^{-1}$ for Mn and 3.0−13.5 $Å^{-1}$ for Nb. Fits to Mn K and Nb K data sets were performed over these k-ranges by using the standard EXAFS equation[40] and a Hanning window (Δk = 2 $Å^{-1}$, ΔR = 0.2 Å). We calculated the EXAFS for undoped tetragonal $BaTiO_3$ from the available crystal structure information (Inorganic Crystal Structure Database ICSD-67520) as the starting model. A second calculation was performed, where the neighboring Ti atoms were replaced by Mn and Nb. In both calculations, the central Ti atom was replaced with Mn (or Nb) while fitting the Mn K (or Nb K) edge data. While this approach allows us to estimate the Ti:(Mn + Nb) ratio at B-sites, the observed uncertainty limits were ∼5%, higher than the doping interval (2.5%). Thus, the final fits were performed by fixing the Ti:(Mn + Nb) ratio to their nominal values. A minimum of two metal (M)−O (M = Mn, Nb) paths were required to describe the O-shell, two M−Ba paths for the Ba-shell and two paths for the next-neighbor B-site: one Ti−Ti single scattering and one Ti−Ti−O multiple scattering path, which amounts to a large number of free parameters. Therefore, the number of free parameters were minimized by four approaches: (1) estimating the S_0^2 values for Mn and Nb individually and by using them as constant

https://doi.org/10.1021/acs.jpcc.1c02539
J. Phys. Chem. C 2021, 125, 14910−14923

values for simultaneous fits, (2) choosing a single ΔE_0 parameter (to align the energy grid of the calculation to that of the data) for all the FEFF paths for a given BTMNO composition, (3) independently estimating the coordination numbers (N) for first shell (N = 6 for O), second shell (N = 8 for Ba), third shell (N = 6 for M = Ti, Mn, Nb), and multiple scattering paths (N = 8) and fixing them; (4) using one isotropic expansion factor (α_1) for the two M−Ba distances (M−Ba1 and M−Ba2) and a second isotropic expansion factor (α_2) for Ti−Ti single scattering and Ti−Ti−O multiple scattering paths. The α_1 and α_2 parameters have been translated into the corresponding bond distances and tabulated. The estimated bond distances and coordination numbers tally very well with the reported crystallographic data on tetragonal $BaTiO_3$ structure (ICSD-67520), which gives us confidence about the high data quality in the present case. The errors were estimated by a standard Levenberg−Marquardt, nonlinear minimization of the statistical χ^2 parameter, built within the Artemis program.[40] Fits to all data in k and R (real part and magnitude) space, extracted EXAFS parameters and their associated error limits are detailed in the Supporting Information.

Theory. Density functional theory (DFT) calculations were performed within two contexts: to extract the theoretical ground state geometries by using three different functionals (PBE, PBE0, and B3LYP) and to assist in the assignment of Raman bands by applying linear response DFT. The phonon modes in $BaTiO_3$ were obtained with periodic calculations in Crystal17[42,43] using the general gradient approximation (GGA) functional PBE and hybrid DFT with the PBE0 and B3LYP functionals. Consistent Gaussian basis sets of triple-zeta valence with polarization quality[44] were utilized for Ti and O, while a scalar relativistic Hay and Wadt small core effective potential[45] and 10 electron valence description[46] were used for Ba. A mesh of 12 × 12 × 12 k points in reciprocal space was generated according to the Monkhorst−Pack method[47] and used for both the geometry optimizations and linear response calculations. The geometry optimizations were performed for both the cell and atoms by using a SCF energy convergence limit of 10^{-8} hartree. Linear response DFT calculations were subsequently performed on the geometry-optimized structures where both the dielectric tensor and vibrational modes were extracted. The Raman intensities were calculated by a coupled-perturbed Kohn−Sham calculation up to fourth order before the calculation of the frequencies as implemented in Crystal17.[48]

RESULTS AND DISCUSSION

Modeling BTO. To provide a thorough basis for the discussion, we performed density functional theory (DFT) calculations of the parent compound ($BaTiO_3$) using three different functionals: one with a pure generalized gradient approximation, GGA (PBE), and two hybrid-functionals (PBE0 and B3LYP). The theoretical ground state was fully geometry-optimized for both cubic and tetragonal cell dimensions and internal atomic coordinates, while subsequent linear response DFT calculations provided the dielectric tensor (Table 1) with naturally slightly lower value along the polar direction in comparison to the less polar directions. To faithfully assign experimental effects arising from asymmetries, such as off-centering, full vibrational assignments were performed by analyzing the displacement vectors and their relative amplitudes. The linear response DFT calculations and the Raman-active vibrational modes can be seen in Table 2. The Raman intensities were extracted by using the Berry phase method using a coupled-perturbed Kohn−Sham calculation approach to fourth order before the calculation of the frequencies.

Table 1. Ground State Structure, Dielectric Tensor, and Band Gap of Cubic (*Pm*-3*m*) and Tetragonal (*P*4*mm*) $BaTiO_3$ Obtained in This Work

	PBE	PBE0	B3LYP	exp[a,b]
		cubic (*Pm*-3*m*)		
a (Å)	4.019	3.978	4.021	4.006
ε_{11}, ε_{22}, ε_{33}	6.476	5.184	5.337	(5.4)
E_g (eV)	1.71	3.79	3.33	3.3
		tetragonal (*P*4*mm*)		
a (Å)	3.997	3.959	3.983	4.000[a] (3.986)[b]
c (Å)	4.136	4.092	4.225	4.018 (4.026)
c/a	1.035	1.034	1.061	1.005 (1.010)
δ_z(Ti)	0.025	0.025	0.016	0.018 (0.015)
ε_{11}, ε_{22}	6.057	4.906	5.188	5.19[c]
ε_{33}	5.169	4.456	4.879	5.05[c]
E_g (eV)	1.76	3.89	3.39	3.4[d]

[a]*Acta Crystallogr., Sect. B: Struct. Sci.* **1992**, *48*, 764. [b]Shirane, G.; Danner, H.; Pepinsky, R. *Phys. Rev.* **1957**, *105*, 856. [c]Hermet, P.; Veithen, M.; Ghosez, Ph. *J. Phys. Condens. Matter* **2009**, *21*, 215901. [d]Wemple, S. H. *Phys. Rev. B* **1970**, *2*, 2679.

Table 2. Calculated and Experimental Raman Active Γ-Point Phonon Frequencies and Dominating LO Phonons from the TO-LO Split for the Tetragonal (*P*4*mm*) Phase of $BaTiO_3$ (in cm^{-1})

Raman mode	PBE	PBE0	B3LYP	exp[a]	exp[this work]
$1A_1/2E$	165	180	187	168	
2E	170	196	187	168	
$2A_1$	291	376[b]	258	270	270
3E	297	313	310	270−320[c]	270−320[c]
B_1	291	313	315	304	308
4E	466	499	494	470	515
$3A_1$	546	569	512	515	515
E TO−LO split	658	717	709	715	720
A_1 TO−LO split	725	777	733	715	720

[a]Raman spectrum of $BaTiO_3$. Parsons, J. L.; Rimai, L. *Solid State Commun.* **1967**, *5*, 423−427. [b]This mode was found at unusually high wavenumbers by using the PBE0 functional. [c]Peak hidden by other stronger vibration modes in the region noted.

All functionals give the well-known overdetermination along the c-axis and thus a slight elongated tetragonal structure in agreement with previous theoretical calculations.[49] Incorporation of exchange via hybrid functionals enables theoretical description that match the experimental situation better than the pure GGA. In addition, the relative off-centering of Ti in the unit cell and the dielectric tensor is best described by B3LYP. The general trends and main conclusions, however, can without loss of generality also be performed from the vibration modes found for the other functionals (Table 2). By use of the B3LYP functional, cubic $BaTiO_3$ exhibits a triply degenerate Ti-displacement mode with compensating Ti−O

https://doi.org/10.1021/acs.jpcc.1c02539
J. Phys. Chem. C 2021, 125, 14910−14923

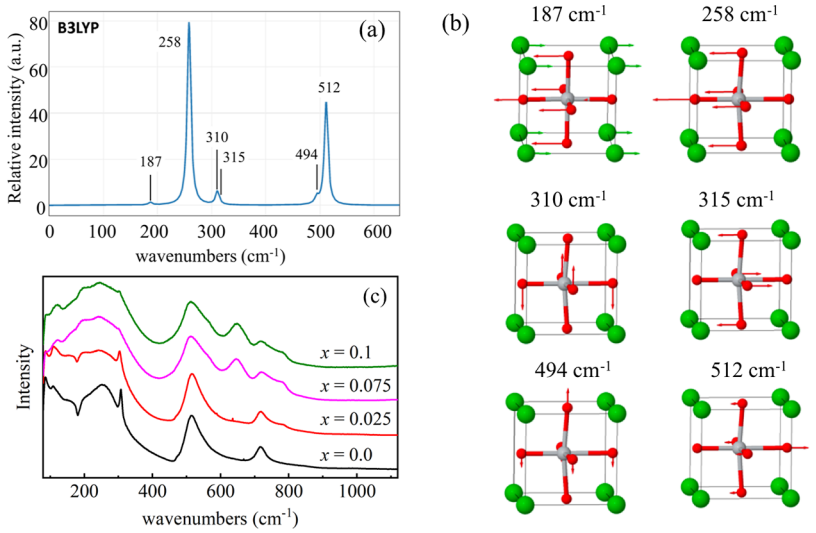

Figure 1. (a) Calculated Raman spectra for tetragonal (*P4mm*) $BaTiO_3$ with the theoretical wavenumbers with the B3LYP functional. (b) Schematic representation of the eigenvectors of the Raman active phonon modes shown in the Ti-centered $BaTiO_3$ perovskite unit. (c) Experimental Raman spectra for the BTMNO series: x = 0.0 (black), 0.025 (red), 0.075 (magenta), and 0.1 (olive).

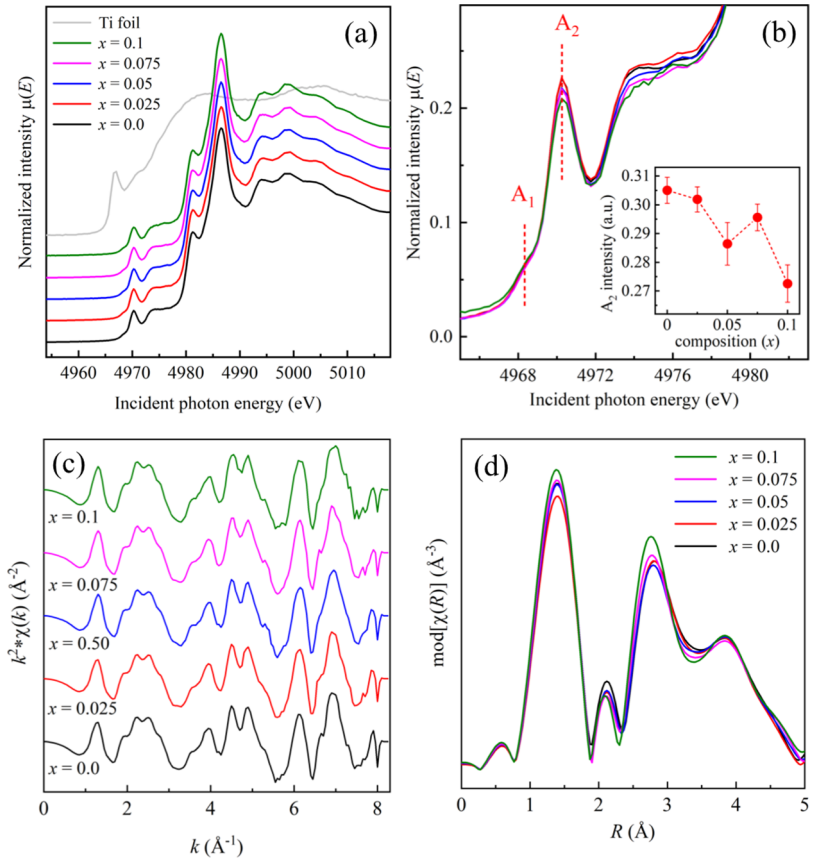

Figure 2. (a) Ti K XANES for the BTMNO series: x = 0.0 (black), 0.025 (red), 0.05 (blue), 0.075 (magenta), and 0.1 (olive), showing Ti^{4+} oxidation states. (b) Pre-edge region showing intense p−d peaks (A_2) in BTMNO samples due to Ti off-centering within O_6 octahedra; the inset shows A_2 peak intensities decreasing with doping, suggesting loss of polarization. (c) k^2-weighted $\chi(k)$ functions and (d) modulus of the $\chi(R)$ functions for Ti data, showing remarkable similarities in Ti local environments in BTMNO systems.

asymmetric stretch at 92 cm^{-1} and a triply degenerate Ti-displacement with more or less constant Ti−O distance but instead compensating Ti−O bending and Ba displacement at 180 cm^{-1}. Two triply degenerate vibrations are found at 326 and 508 cm^{-1} which correspond to asymmetric O−Ti−O bending and symmetric bending, respectively, where the latter is coupled to an asymmetric O−Ti−O stretch. The vibrations at 92, 180, and 508 cm^{-1} are IR-allowed with the first mode having high intensity. The 180 cm^{-1} mode has more or less negligible intensity due to the small change in dipole during the vibration, while the 508 cm^{-1} vibration should have a small but detectable intensity due to the induced dipole change upon

https://doi.org/10.1021/acs.jpcc.1c02539
J. Phys. Chem. C 2021, 125, 14910−14923

the Ti−O vibration coupling. Neither of the modes are Raman-active, however, due to the cancellation of changes in polarizability during the vibration from the selection rules of a cubic perovskite system.

The off-centering of Ti in the transition to a tetragonal system activates several of the vibrations due to the broken symmetry. For the tetragonal phase, the 180 cm^{-1} mode in the cubic system is translated to 187 cm^{-1}, and the triply degenerate 326 cm^{-1} mode in the cubic system splits into a high intensity 258 cm^{-1} mode and a doubly degenerate mode at 310 cm^{-1}. The triply degenerate 508 cm^{-1} mode in the cubic system is transformed into a doubly degenerate mode at 494 cm^{-1} and a nondegenerate mode at 512 cm^{-1}. The theoretical Raman spectrum with the B3LYP functional and the displacement for the eigenvectors of the elements in the unit cell for the tetragonal phase ($P4mm$) is shown in Figure 1a,b. As is well-known, the dipoles that are created with long-wave longitudinal phonons in polar crystals are responsible for the removal of degeneracy between the LO and TO phonons at the Brillouin zone center and thus the phenomenon of LO−TO splitting. Because the magnitude of the TO−LO split is dependent on the dielectric constant, a hybrid functional is here preferred due to the inclusion of more exact exchange and thus closer correspondence between the experimental and theoretical dielectric properties. By use of the Born effective charges and the theoretical dielectric tensor, subsequent linear response calculations were utilized to obtain LO phonons. Using the B3LYP functional, we calculated the LO modes to 184 cm^{-1} (E(LO)), 196 cm^{-1} (A_1(LO)), 310 cm^{-1} (E(LO)), 482 cm^{-1} (E(LO)), 486 cm^{-1} (A_1(LO)), 709 cm^{-1} (E(LO)), and 733 cm^{-1} (A_1(LO)), where only the latter two have high intensities. For the comparison of the vibrational modes using different DFT functionals and experimental modes, see Table 2.

Experimental Raman Spectra. Figure 1c shows the Raman spectra of $BaTiO_3$ (x = 0.0) and BTMNO samples for x = 0.025, 0.075, and 0.1. Upon comparison with the theoretical spectra for the tetragonal structure with that of the experimental $BaTiO_3$, it is clear that the experimental spectrum is more complex and contains more asymmetric as well as broader modes. Moreover, the complexity of the spectra increases further with doping. The Raman spectrum shows broad peaks centered around 270 cm^{-1} ($2A_1$, E(TO)), a sharp peak at 308 cm^{-1} (B_1, E(LO + TO)), an asymmetric broad peak at 515 cm^{-1} (A_1, E(TO)), and a broad weak peak at 720 cm^{-1} (A_1(LO), E(LO)), where phonon mode assignments are given inside parentheses. A_1 modes are related to Ti ion displacements relative to O and Ba ions along the c-axis and E modes to Ti ion displacements along the a/b-axis, while B_1 modes are related to O ion displacement along the c-axis.[50] The presence of the E(1TO) soft mode is a fundamental criterion for spontaneous polarization to exist through long-range phenomenon, which indicates the existence of ferroelectric properties in BTMNO samples. It increases in relative intensity as x increases; that is, the volume fraction of the B-site exhibiting an asymmetric breathing mode increases with x, which provides direct evidence[51] of B-site doping of Mn and Nb. One can note that the asymmetric shoulder of the 515 cm^{-1} band develops with increased doping. Recalling the mode assignment from DFT (Figure 1a), the JT distorted Mn−O_6 octahedra and off-centered Nb−O_6 octahedra are seen to distort the symmetric bending modes in the Ti−O_6 octahedra in the doped samples compared to pure $BaTiO_3$.

One can also note a new band emerging at around 645 cm^{-1} with an accompanying band at around 800 cm^{-1} with intensity at the expense of the intermediate band at 720 cm^{-1} (Figure 1c), further supporting the broken symmetry modifying the TO−LO split upon Ti replacement. The origin of this is due to incorporation of heavier B-site cations and changed bond strength of the metal−O bond. The line shapes at lower wavenumbers also become visibly broader at higher concentrations (7.5% and 10%), as more Ti sites are being substituted by Mn and Nb ions.

Ti K XAS. The absolute absorption energy (E_0) for a specific X-ray edge can be used to fingerprint the mean valence for an element when compared to well-known standards. Figure 2a shows the normalized Ti K XANES for the BTMNO series and Ti foil. The E_0 positions, as estimated from the position of the inflection point in the main part of the absorption Ti K-edges for all BTMNO samples, show extremely consistent values close to 4987 eV, indicating a Ti^{4+} oxidation state. Figure 2b shows the pre-edge region of the Ti K XANES for BTMNO samples, exhibiting multiple peaks,[52,53] of which the first two peaks (A_1 and A_2) are marked. While peak A_1 is explained by a quadrupolar 1s → 3d transition, peak A_2 has contributions from both quadrupolar (1s → 3d) and dipolar (1s → 4p) transitions, the quadrupolar transition being the more dominant one.[52,53] In tetragonal $BaTiO_3$, Ti atoms are displaced from the center of O_6 octahedra, thereby breaking the centrosymmetry and affecting p−d mixing. A_2 peak intensity is therefore an indicator of the degree of orbital hybridization between the two atomic states and is directly proportional to the mean-squared displacements of Ti from the centers of the surrounding O_6 octahedra. The A_2 peak is difficult to model with a single Gaussian over a narrow window due to significant overlap with the intense peaks beyond 4972 eV (Figure 2b). Thus, a much wider pre-edge region (∼15 eV) is needed to be modeled for a more accurate estimate of A_2 peak intensity variations as a function of doping (x). Pre-edge fine structure fits over −20 to −5 eV across the Ti K absorption edge of the BTMNO series were performed, after proper background subtraction using a linear baseline and a Lorentzian function. The background subtracted data, corresponding total fits, and contributions of individual Gaussian components to the total fit for all BTMNO samples are plotted in Figure S1, and the fit parameters are tabulated in Table S2. A_2 peak intensities derived from the fits are plotted in the inset of Figure 2b. We find A_2 intensities to decrease with co-doping Mn and Nb at Ti sites, suggesting reduced p−d mixing.

Increased doping systematically decreases tetragonality and, hence, the polarization in $BaTiO_3$. The largest drop is noticed going from x = 0.075 to x = 0.1, where the system becomes a paraelectric (cubic). Nonetheless, Figure 2b clearly establishes that in BTMNO Ti ions remain off-centered within the Ti−O_6 octahedral environment in $BaTiO_3$ for all doping concentrations; the extent of this distortion decreases with x.

Figure 2c shows the k^2-weighted $\chi(k)$ functions for Ti. We find remarkable similarities in Ti local environments, suggesting the Mn and Nb dopants to have little influence on the overall Ti environment. Ba L_3 (5247 eV) XAS interferes strongly with Ti K (4966 eV) XAS, limiting reliable data for Ti K only up to k_{max} ∼ 8.2 $Å^{-1}$. The number of independent variables (n) that could be extracted is defined by the resolution of EXAFS as $\approx 2\Delta k \Delta R/\pi$. For Ti K, n gets reduced to only 3, far short of minimum requirement n = 7 to estimate

https://doi.org/10.1021/acs.jpcc.1c02539
J. Phys. Chem. C 2021, 125, 14910−14923

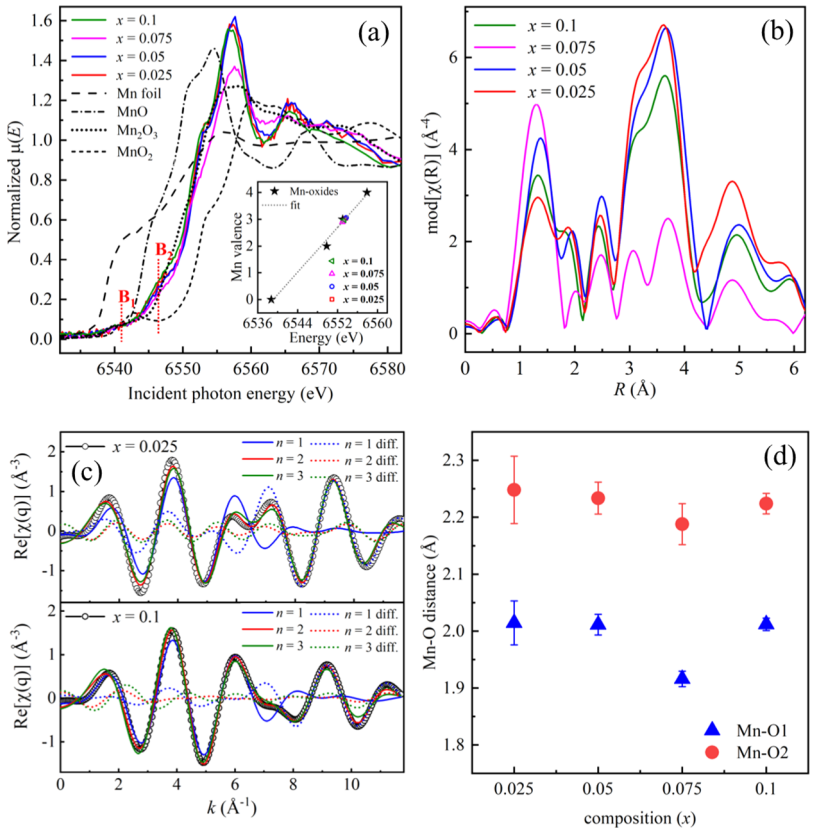

Figure 3. (a) Mn K XANES for the BTMNO series: x = 0.025 (red), 0.05 (blue), 0.075 (magenta), 0.1 (olive), and well-known Mn standards; inset shows Mn in BTMNO systems to assume 3+ formal valence. (b) Modulus of the k^3-weighted $\chi(R)$ functions for Mn data. (c) Mn−O shell modeled with different numbers (n) of Mn−O distances: 1 (blue), 2 (red), and 3 (olive) and corresponding differences plotted in dotted lines. (d) Mn−O distances within Mn−O_6 octahedra, showing four short Mn−O1 (blue triangles) and two long Mn−O2 (red circles) bonds, suggesting JT distortion within the Mn^{3+}−O_6 octahedra.

Ti off-centering in the Ti−O_6 octahedra. The modulus of Fourier transforms of $\chi(k)$ over the range 2.0−8.0 $Å^{-1}$ for the Ti K-edge data is shown in Figure 2d. A small increase of amplitude is noticeable for the x = 0.1 (olive) sample, suggestive of somewhat lower extent of distortion in the Ti local environment. This increase is be expected from decreasing tetragonality of the system with doping (Figure 2b), which eventually becomes cubic at x = 0.1.

Mn K XAS. Figure 3a shows the normalized Mn K XANES for the BTMNO series in comparison with reference Mn oxides [MnO(II), Mn_2O_3(III), and MnO_2(IV)] and Mn foil. A linear fit to the estimated E_0 positions of the Mn standards was used to extract the Mn valence states by mapping the E_0 positions of the BTMNO system: 6553.66 ± 0.11 eV for x = 0.025, 6553.73 ± 0.07 eV for x = 0.05, 6552.98 ± 0.11 eV for x = 0.075, and 6553.35 ± 0.03 eV for x = 0.1. The E_0 values for all BTMNO samples show a narrow spread around the Mn_2O_3 standard (6553.02 ± 0.03 eV), indicating a Mn^{3+} oxidation state (Figure 3a, inset). The E_0 value also agrees well with the reported[54] E_0 value for the Mn K-edge in $LaMnO_3$, another perovskite structure with Mn^{3+} residing in an octahedral O environment. The leading Mn K-edge for the 7.5% sample is slightly broader. While mixed valence states are known to induce such broadening, the leading edge is still positioned significantly apart from MnO and MnO_2. The observed broadening therefore is related to the higher disorder present in the x = 0.075 sample.

The quadrupolar transitions (Mn 1s → 3d (t_{2g}) and 3d (e_g) states) in the Mn K pre-edge appear as a broad feature in the region B_1 which could not be resolved experimentally due to core-hole lifetime broadening. The intensity of feature B_1 for Mn is much lower compared to the corresponding quadrupolar intensities observed for Ti (Figure 2a) for any given x value. The Mn−O_6 octahedra, therefore, are expected to be relatively more symmetrically distorted than Ti−O_6 octahedra. The feature in region B_2 (Figure 2a) corresponds to the d-states of neighboring metal (M) sites through oxygen-mediated intersite hybridization of Mn(4p)−O(2p)−M(3d). Feature B_2 shows small, non-monotonic changes with doping, which might be a consequence of disorder associated with B-site doping, to be discussed later.

Figure 3b shows the Fourier transform of $\chi(k)$ (2.0−9.0 $Å^{-1}$) for the Mn K-edge data in the BTMNO series. The first split peak at ∼1.5 Å corresponds to nearest O neighbors, and the multipeak at ∼3.2 Å corresponds to second (Ba) and third near neighbors (Ti, Mn, and Nb), including multiple scattering contributions from Mn−Ti−O paths. The apparently lower values of the distances are due to phase shifts for different atom-pair correlations and were accounted for during the fitting procedure. The Mn−O peak amplitude tends to decrease with doping, indicating that the oxygen environment around the manganese is becoming more distorted, except for the x = 0.075 sample. The multipeak corresponds to a weighted sum of contributions from Mn−Ti, Mn−Mn, and Mn−Nb. This peak appears much smoother, which suggests

https://doi.org/10.1021/acs.jpcc.1c02539
J. Phys. Chem. C 2021, 125, 14910−14923

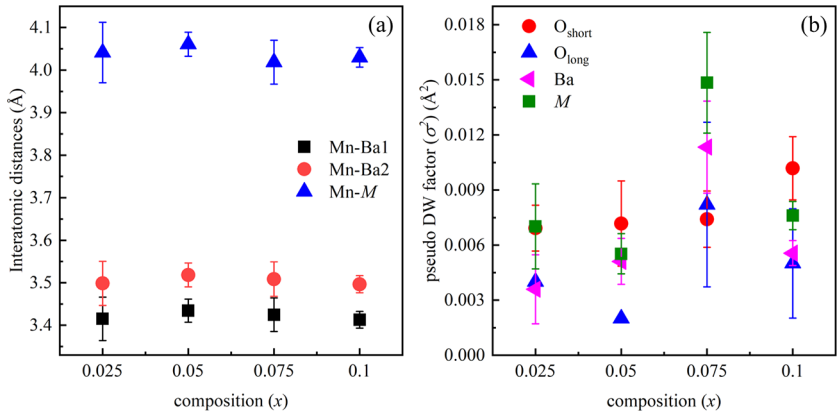

Figure 4. (a) Mn−Ba (2NN) short (black squares), Mn−Ba long (red circles), and Mn−M (M = Ti, Mn, Nb) (3NN) (blue triangles) interatomic distances in BTMNO samples. (b) Pseudo-Debye−Waller factors (σ^2) associated with each sublattice: O (short: red circles, long: blue triangles), Ba (magenta left triangle), and M (olive squares), revealing high σ^2 values and the largest scatter for the x = 0.075 composition.

that the distribution of Mn−Ti, Mn−Mn, and Mn−Nb interatomic distances is possibly more disordered. Hence, no large changes are observable in the local structure in this bond length range for this peak with doping. The x = 0.075 sample breaks this trend, with a very different higher shell environment and possibly higher disorder.

We found the optimal number of O atoms surrounding Mn to be 6 for all x, clearly establishing B-site doping of Mn. The split peak on Mn−O prompts us to check for multiple Mn−O distances within the Mn−O_6 octahedra in a perovskite structure. In this framework, the quality of preliminary fits with different Mn−O distances (n = 1, 2, 3) and one σ^2 parameter was compared (Table S3) and presented in Figure 3c for the lowest and highest doping concentrations (2.5% and 10%). The residuals (dotted lines) obtained considering multiple Mn−O distances (n = 2, 3) were significantly lower (by a factor between 20% and 30%) (Figure 3c) than the residuals calculated with a single Mn−O bond distance (n = 1), as reflected in lower fit quality of the n = 1 models. Also, the n = 1 models consistently yielded higher σ^2 values (Table S3) compared to n = 2, 3 models, suggesting the O_6 environment surrounding Mn to be nonisotropic. The systematic lower residual for n = 2 compared to n = 3 indicates that the Mn−O_6 octahedra in BTMNO systems support the model with two different values of the Mn−O distance: four short (Mn−O1) and two long Mn−O (Mn−O2) bonds. Formation of such distorted O shell due to B-site doping was evidenced in our Raman experiments (Figure 1c) as well. The two different Mn−O bonds are plotted in Figure 3d which does not show any noticeable composition dependence. Fits to the Mn K-edge data over the range Δk = 2.0−9.0 Å^{-1} and ΔR = 1.05−4.0 Å for the BTMNO series are provided in the Supporting Information (Figure S2a,b). EXAFS parameters corresponding to first shell (Mn−O) fits are provided in Table S4.

Different types of distortions could be prevalent in the Mn−O_6 octahedra: JT effect, Mn off-centering within O_6 octahedra, charge disproportionation, and occurrence of multiple Mn^{3+} sites. Each of these effects would have a different manifestation on the structure, as mentioned below:

- The Jahn−Teller (JT) effect would (e.g., similar to $LaMnO_3$) generate a 2 + 2 + 2 distribution of Mn−O distances at ∼1.9, ∼1.97, and ∼2.15 Å along three different crystallographic axes in an orthorhombic[54] structure, represented as JT-(o). In a tetragonal[55] structure, JT distortion (JT-(t)) is expected to generate a 4 + 2 distribution of Mn−O distances (∼1.9 and ∼2.15 Å): two along the axis of distortion and four in the plane perpendicular to the axis of distortion.
- Off-centering (OC) distortion[56] of Mn along the polar c-axis like Ti would create a 1 + 4 + 1 distribution of Mn−O distances: one short and one long Mn−O axial bond (along c) and four Mn−O bonds (in the ab-plane) assuming intermediate values.
- Charge disproportionation (CD) of a fraction (y) of Mn^{3+} into Mn^{2+} and Mn^{4+} would create $y \times Mn^{3+}$−O distances ∼2 Å, $(1 - y/2) \times Mn^{2+}$−O (∼2.14 Å) and $(1 - y/2) \times Mn^{4+}$−O bonds at ∼1.87 Å.[57]
- Mn^{3+} can exist as multiple sites (MS), where the short and long Mn−O bonds are associated with two different sites.[58] EXAFS can be effectively employed to resolve such local distortions, as revealed by the simulations provided in Figure S3.

The bond lengths used in the bullets above are based on sum of atomic radii[57] and ignores doping-induced lattice effects. However, for BTMNO these approximations are not too crucial due to rather comparable ionic radii of the dopants (Mn^{3+}: 0.72 Å and Nb^{5+}: 0.78 Å) replacing Ti^{4+} (0.745 Å) and low doping concentrations.

Both OC and CD effects would necessarily require the ratio of long and short Mn−O bonds to be 1:1, which is in sharp contrast to ratio (1:2) we found find from optimized fits (n = 2) to the Mn-EXAFS (Figure 3d). MS are known to occur in solid solutions with large ionic radii differences between the substituted and substituting ions and at high doping limits. Such ionic radii mismatch induces strain that can yield locally heterogeneous phases, often tracked by isosbestic points[58,59] in the metal K absorption edges. No signature of isosbestic points could be detected in the Mn K XANES (Figure 3a), thereby making the MS model rather unlikely as well. This is not surprising, considering similar ionic radii of the host (Ti^{4+}) and the dopant (Mn^{3+} and Nb^{5+}) ions and such low doping concentrations, as the EXAFS would be dominated by scattering from Ba and Ti, which predominantly form the matrix. Our results in Figure 3d with n = 2 (four short and two long Mn−O bonds) therefore can be best related to a Jahn−Teller distortion (JT-(t)). The Mn−O environment in BTMNO is in marked contrast with the Mn−O arrangement

https://doi.org/10.1021/acs.jpcc.1c02539
J. Phys. Chem. C 2021, 125, 14910−14923

in orthorhombic $LaMnO_3$ which experiences a JT-(o) distortion. This is primarily due to tetragonal symmetry of $BaTiO_3$, having identical Ti−O−Ti angles along a- and b-axes (∼180°). At low doping limits of Mn, the B-site is mostly Ti, leading to more regular arrangement of Mn−O bonds along the a- and b-axes.

For a tetragonal structure one expects a bimodal distribution of the second shell (Mn−Ba) and third shell (Mn−M; M = Ti/Mn/Nb) distances. Scattering factors of Mn and Ti are rather similar, while Nb has a significantly different scattering factor. However, the dopant concentration limit is too low to independently estimate the (Mn + Nb):Ti concentration. Therefore, the nominal (Mn + Nb):Ti ratio was used as a constraint to model the higher neighboring shells. Details of the corresponding Mn K EXAFS parameters are provided in the Supporting Information (Table S5). Figure 4a shows the variation of Mn−Ba and Mn−M distances with x. The distances remain roughly similar, with no appreciable composition dependence. The σ^2 values corresponding to all the different sublattices are shown in Figure 4b across the entire composition window. Clearly the σ^2 parameters assume higher values and reveal the maximum scatter among different sublattices for the x = 0.075 sample. The σ^2 for Mn−M is rather large, suggesting high disorder at the B-sites. Also, we find that the x = 0.075 sample experiences the largest JT splitting (Figure 3d) and broadening of the Mn K absorption edge (Figure 3a). All these observations are clearly suggestive of a unique, more disordered Mn local environment for the x = 0.075 sample.

Nb K XAS. Figure 5a shows the normalized Nb K XANES for the BTMNO series. Similar to the Mn co-dopant, we find that the E_0 positions (white line energy absorption feature due to the 1s → 4p transition) stay more or less constant for all doping concentrations. The BTMNO samples show similar values (∼18903 eV), closest to the reported value[60] for Nb_2O_5, indicating Nb to exist predominantly as Nb^{5+} at these time scales (10^{-15} s). A single broad, intense pre-edge shoulder feature (labeled C) around 18990 eV is noticeable, but the fine structure cannot be resolved due to the large intrinsic width of the Nb core level. Nonetheless, considerable intensity of the p−d peak indicates the niobium atoms to be displaced from the centers of the NbO_6 octahedra.[32,61,62] The baseline-subtracted Nb K absorption edge of the BTMNO series over −15 to −5 eV is shown in the inset of Figure 5a. The peak intensity is maximum for the x = 0.075 sample, suggesting Nb distortion within the O_6 octahedra is expected to be largest for this composition.

Figure 5b shows the modulus of $\chi(R)$ obtained by Fourier transformation over the k-range 3.0−13.5 $Å^{-1}$. Direct comparison of first peak (O shell) in $\chi(R)$ suggests that the oxygen polyhedra around Nb ions remain similar regardless of the doping concentrations, except for x = 0.075. The Nb−O peak distribution is narrower compared to the distribution for the co-dopant Mn (Figure 3b), suggesting that the oxygen environment around the Nb is possibly less distorted compared to Mn when occupying a Ti site. The intense multipeak at ∼3.2 Å corresponds to combined scattering from Ba, Ti, Mn, and Nb and a significant multiple scattering path Nb−Ti−O described already. No significant changes in the peak profile can be noticed in this bond length range with x, except for the x = 0.075 sample which exhibits higher disorder.

The coordination number for O atoms was found to be 6, indicating that Nb acts as substitutional impurity at Ti sites in

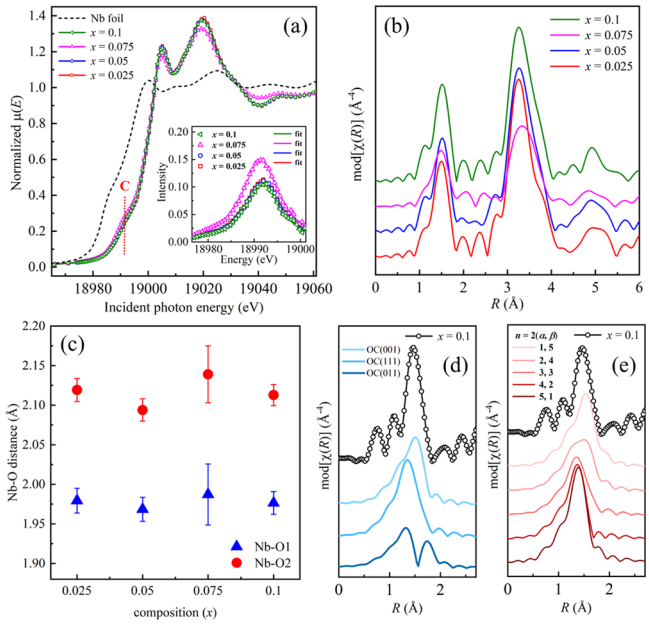

Figure 5. (a) Nb K XANES for the BTMNO series: x = 0.025 (red), 0.05 (blue), 0.075 (magenta), and 0.1 (olive); inset shows the baseline-subtracted pre-edge feature C related to local distortion of Nb within the O_6 octahedra. (b) Modulus of $\chi(R)$ for the BTMNO series (c) Distribution of Nb−O bond distances within Nb−O_6 octahedra, showing one short Nb−O1 (blue triangles) and five long Nb−O2 bonds (red circles). (d) Nb−O shell for 10% Mn-Nb-doped $BaTiO_3$ compared with different models: Nb off-centering models along (001), (111), and (011) directions. (e) All possible combinations for the n = 2 (α, β) model, revealing closest proximity of the (α = 5, β = 1) model to the OC(001) model, i.e., off-centering distortion of Nb within the Nb^{5+}−O_6 octahedra.

BTMNO. The intense p−d peak (Figure 5a) and Nb−O peak structure (Figure 5b) prompt us to check for possible distortions within the Nb−O_6 octahedra. As observed with Mn−O_6, the n = 1 model (single Nb−O distance) could not provide a satisfactory description of the Nb−O_6 octahedra. The Nb−O octahedron was therefore modeled with multiple distinct Nb−O paths (n = 2, 3). Both models yielded similar quality fits, but the results were not unique. This is because all three-path models (n = 3) approached a five short Nb−O and one long Nb−O bond combination of the two-path (n = 2) model. Optimal fits were thus concluded by using two Nb−O distances, five short (Nb−O1), and one long (Nb−O2). This unusual bonding arrangement Nb−O_6 octahedra persists for all doping compositions up to x = 0.1, as plotted in Figure 5c. Fits to the Nb K-edge data over the range Δk = 3.0−13.5 $Å^{-1}$ and ΔR = 1.05−4.0 Å for the BTMNO series are provided in Figures S4a,b. EXAFS parameters corresponding to first shell (Nb−O) fits are provided in Table S6.

Nb^{5+} being a d^0 ion is JT-inactive; therefore, the Nb−O environment was checked for plausible distortions other than JT:

- Off-centering (OC) distortion[30−32,63] of Nb along (001), (011), or (111) directions.
- OC (001) would create a 1 + 4 + 1 Nb−O bond distribution, as explained previously.
- OC (011) would create three sets of Nb−O distances, two small, two intermediate, and two large Nb−O bonds (2 + 2 + 2 distribution) typical of an orthorhombic distortion in a perovskite.

https://doi.org/10.1021/acs.jpcc.1c02539
J. Phys. Chem. C 2021, 125, 14910−14923

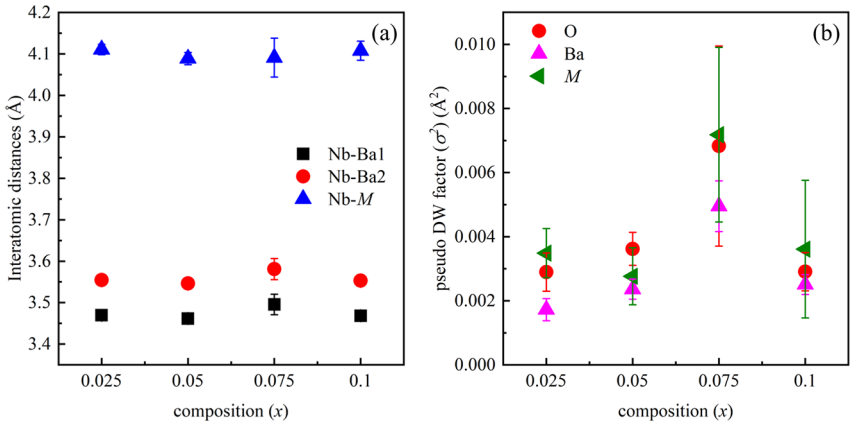

Figure 6. (a) Nb−Ba (2NN) short (black squares), Nb−Ba long (red circles), and Nb−*M* (*M* = Ti, Mn, Nb) (3NN) (blue triangles) interatomic distances in BTMNO samples. (b) Pseudo-Debye−Waller factors (σ^2) associated with each sublattice: O (red circles), Ba (magenta left triangle), and *M* (olive squares), showing high σ^2 values and largest scatter for the x = 0.075 composition.

- OC (111) would create two sets of Nb−O distances each involving three bonds (3 + 3 distribution), typical of a rhombohedral distortion in a perovskite.
- Charge disproportionation (CD) would have a different interpretation for Nb than Mn. This is because Nb is already presumably at its maximum valence (+5), but it can assume a range of lower formal valence states. This would be reflected as a weighted sum of different fractions of Nb^{n+}−O bonds at different distances (e.g., Nb oxides).
- Multiple sites (MS)[58] can exist, one site associated with only short Nb−O bonds and the other site with only long Nb−O bonds.

To fit a five short and one long Nb−O bond length description, a CD model would require assigning 83.3% of Nb−O bonds to Nb^{5+} and 16.7% to Nb^{4+}, resulting in nonstoichiometry effects. No appreciable broadening of the main Nb K absorption edge has been observed for BTMNO samples to support this claim. Rather, the absorption profiles are almost overlapping, suggesting the fraction of Nb^{5+} in Nb sites has no dependence on concentration. For a MS model, a similar case can be argued as with Mn that this mode of distortion, even if operative, would be rather weak at such low doping levels. We also find no evidence for isosbestic points in the Nb K XANES to support the CD or the MS model. Moreover, these models cannot explain the intense pre-peak in Nb K XANES. The Nb−O_6 distortion must therefore be related to some form of OC distortion in the Nb−O_6 octahedra.

Figure 5d compares all OC three-path models (n = 3). The OC (011) model is simply too broad to describe the Nb−O_6 environment, The OC (111) model, too, yielded a poor description with largely offset Nb−O bond distances. Thus, Nb is not likely to be displaced toward any of the Nb−O_6 octahedral faces or edges. The OC (001) model improves the description reasonably, hinting that the Nb−O_6 comprises of a considerable fraction of shorter Nb−O bonds, assuming values close to the Ti−O distances in the *ab*-plane for $BaTiO_3$. In undoped $BaTiO_3$, an ideal Ti off-centering along (001) gives rise to three Ti−O distances of 1.84, 1.98, and 2.14 Å. If we simply replace the Ti by Nb and use a single expansion factor (retaining proportional variation of the Ti−O bond lengths in $BaTiO_3$), the corresponding Nb−O distances occur around 1.84, 1.97, and 2.11 Å, with poor fit quality. The short Nb−O bond, when relaxed, immediately converges to a value ∼1.98 Å, and a high fit quality is achieved. Interestingly, this value is almost identical to the four equatorial Ti−O distances. So essentially, one sees a distribution of five short and one long Nb−O distance within the Nb−O_6 octahedra. Interestingly, the longer Nb−O bond also assumes a value close to the longer axial Ti−O bond in $BaTiO_3$. This implies that although Nb distorts the O_6 cage locally, some portion of the intrinsic tetragonal (001) distortion of the O_6 cage (Ti−O_6 octahedra in pure $BaTiO_3$) is still preserved. Neither of the other two OC models—OC (011) (2 + 2 + 2 distribution) and OC (111) (3 + 3 distribution)—could be reduced similarly to a five short + one long Nb−O distance distribution. The Nb−O_6 distortion we observe, therefore, can be regarded as a structural variant of the OC (001) distortion model.

We check the validity of this observation in Figure 5e by comparing all two-path (n = 2(α, β)) Nb−O bond combinations, where α and β represent the number of short and long Nb−O bonds. One can clearly see that how the Nb−O description could be approached by systematically replacing longer Nb−O bonds (β) with shorter Nb−O (α) bonds. Thus, Nb when doped at the Ti site does remain off-centered within the O_6 octahedra being displaced roughly along the polarization axis. This finding emphasizes the natural tendency of d^0 ions in perovskites to create a polar distortion at the B-site, a fundamental criterion for stabilizing a ferroelectric ground state.[18,25] Thus, apart from being a charge compensator ion, Nb^{5+} also is likely to contribute to the total polarization of the system, although the extent of off-centering is relatively lower as compared to Ti. We note here that local structure about Nb is in marked contrast with Nb−O arrangement in $KNbO_3$ and similar reported structures of Nb in perovskite ferroelectrics. This again is related to the tetragonal symmetry of the $BaTiO_3$ lattice, which drives the directionality of Nb displacement within the Nb−O_6 octahedra.

Figure 6a shows the interatomic distances for second shell (Nb−Ba) and third shell (Nb−*M*; *M* = Ti/Mn/Nb). The (Mn + Nb):Ti ratio was constrained close to the nominal (Mn + Nb):Ti ratio to model the higher neighboring shells, as in the Mn K-edge fits. Details of the corresponding Nb K EXAFS parameters are provided in Table S7. The Nb−Ba and Nb−*M* distances do not reveal any significant changes with increasing doping concentration. The σ^2 values for the different sublattices are shown in Figure 6b for all x values. Like Mn,

https://doi.org/10.1021/acs.jpcc.1c02539
J. Phys. Chem. C 2021, 125, 14910−14923

here also we notice the largest σ^2 values for the x = 0.075 sample, also exhibiting the largest spread of σ^2. The spread of σ^2 among different sublattices, however, is considerably lower compared to the Mn results (Figure 4b).

Doping Comparison and Links to Material Functionality. Comparing the local environments about Mn and Nb reveal several interesting facts. First, the distortions associated with Mn and Nb doping at Ti sites are fundamentally different from each other: Mn at Ti sites show JT distortion, while Nb at Ti sites show off-center distortion. This has important implications on material properties as will be discussed below. Second, doping effects of Mn/Nb are extremely local in nature. Most pronounced structural changes are observed for the nearest neighboring O shell, while the higher shell (Ba, Ti) environments show smaller lattice effects regardless of doping composition, with interatomic distances for Nb being slightly larger (~0.05 Å) than Mn. This suggests that local structural descriptions about dopants in BTMNO samples start conforming toward more uniform description within 4 Å, where the next B-sites occur. The changes in the O environments thus are accommodated by the lattice through cooperative rotation with neighboring Ti−O_6 octahedra, preserving the overall lattice periodicity. Third, the σ^2 values for all sublattices in the Mn local environment are systematically higher compared to the corresponding σ^2 values in the Nb local environment, which explains why the $\chi(k)$ oscillations for Mn are comparatively less structured than Nb-$\chi(k)$ (Figure S5). This can be understood from the changes in the O−O interatomic distances in a Ti−O_6 octahedra when the Ti is replaced by a Mn or Nb. The long O−O interatomic distance for Ti in $BaTiO_3$ is ~4.0 Å. When doped with Mn, the O−O interatomic distance increases to ~4.4 Å, much higher compared to O−O interatomic distance (~4.2 Å) when Ti is replaced with Nb. The larger octahedral volume of Mn−O_6 compared to Nb−O_6 is expected to be compensated through greater adjustment of the Mn−O−Ti bond angles and hence larger σ^2 values. This is not surprising, as JT is known to be a stronger lattice distortion compared to OC.

Incorporation of Mn in $BaTiO_3$ supplies a finite number of d electrons (d^n) that create new midgap states with predominantly Mn 3d character.[28] Our O K XAS studies[29] have also identified newly formed doped states appearing below the conduction band to be primarily of Mn 3d character. By removing the 3d degeneracy, the JT distortion governs the splitting of the midgap states, eventually lowering the bulk band gap. Mn doping, therefore, is primarily associated with improving the photovoltaic functionality of BTMNO. On the other hand, exchanging Ti with Mn is believed to be detrimental to ferroelectricity, as exchanging d^0 ions by d^n ions typically decreases the inherent polarization. However, larger polarization loss (25%) was reported by Das *et al.*[28] when the co-dopant to Nb^{5+} was a JT-inactive Fe^{3+} ($3d^5$) ion. This indicates that strong JT distortions about Mn^{3+} aid effective coupling of Mn^{3+}−O_6 octahedra to the surrounding corner-shared tetragonally distorted Ti−O_6 octahedra, minimizing loss of overall $BaTiO_3$ polarization.

The other dopant, Nb, plays a very different role when doped at Ti sites. An equimolar amount of Nb^{5+} acts as a charge compensator to Mn^{3+}, maintaining overall charge neutrality in BTMNO. The "d^0-ness"[25] of metals occupying B-sites (e.g., Ti^{4+}, Nb^{5+}, and Zr^{4+}) in perovskites is well-known to generate off-centered displacement of the d^0 ion within the O_6 octahedra which stabilizes a ferroelectric phase. We find similar off-centering distortion for Nb^{5+} within the O_6 octahedra for the BTMNO systems. Because of this innate asymmetry, Nb could retain some portion of the polarization of $BaTiO_3$ lost due to Mn doping. However, being a d^0 system, Nb^{5+} is not expected to have any appreciable influence on band gap engineering. Incorporation of Nb, therefore, is primarily associated with the ferroelectric functionality of BTMNO.

The above discussion highlights the effectiveness of co-doping aliovalent ions Mn^{3+} and Nb^{5+} over isovalent doping in broadening the absorption in the visible region for ferroelectric $BaTiO_3$. Isovalent Mn doping alone in $BaTiO_3$ results in a hexagonal structure with no ferroelectricity.[26] Also, an electronically degenerate Mn^{4+} ion would be JT-inactive. Isovalent doping of only Nb in $BaTiO_3$, on the other hand, is synthetically challenging due to slow kinetics of Nb incorporation.[64] It is also known to suffer from charge imbalance and requires high temperature conditions for reproducible electrical properties.[65] In contrast, aliovalent doping of Mn^{3+}−Nb^{5+} pair could behave as a dipole that can effectively couple to the tetragonally distorted $BaTiO_3$ lattice and help retain the overall electric polarization. This explains the efficacy of the co-doping strategy to strike the right balance between good solar absorption and good polarization to be able to function as a potential ferroelectric photovoltaic material.

Figure 7 shows the local structure−property correlation between distortions (δ) within the local octahedra associated

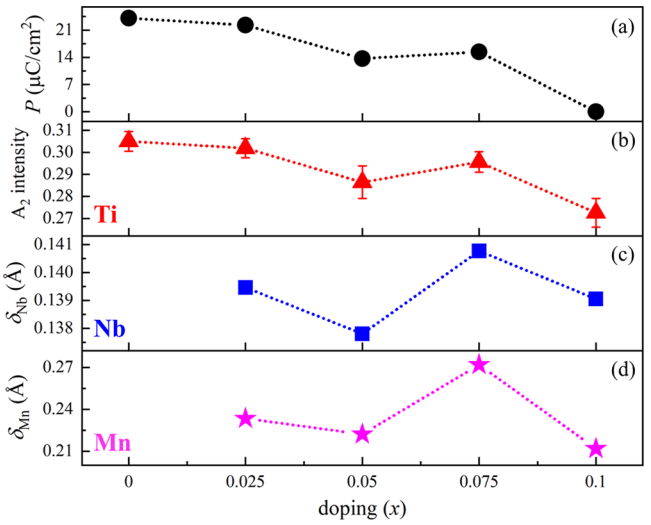

Figure 7. Correlation of (a) polarization (P) (black circles) in BTMNO to structural distortions associated with the B-sites: (b) Ti^{4+} off-centering distortion indicated by A_2 intensities (red triangles), (c) off-centering distortion of Nb^{5+} (blue squares), and (d) Jahn−Teller distortion of Mn^{3+} (magenta stars) ions.

with each B-site in BTMNO and the polarization (P) values reported by Das et al.[28] Using high-energy resolution fluorescence detected X-ray absorption (HERFD-XAS) at the Ti K-edge, we have already elucidated[29] how evolution of the A_2 peak intensities (∝ Ti off-centering) correlates strongly with evolution of P values over the doping window ($0.0 \leq x \leq 0.1$). For the dopants, we define distortion (δ) from the difference of short (M−O1) and long (M−O2) bonds within the respective M−O_6 octahedra (M = Mn, Nb): thus, $\delta M = \Delta M$−O = M−O2 − M−O1. Surprisingly enough, we find that the doping dependence for δ_{Mn} and δ_{Nb} roughly parallels the

https://doi.org/10.1021/acs.jpcc.1c02539
J. Phys. Chem. C 2021, 125, 14910−14923

variation of A_2 intensities and P values. This observation indicates strong coupling of Mn and Nb to the inherent Ti distortion in BTMNO. Replacing Ti^{4+} with Nb^{5+} keeps the number of d^0 ions maximum to retain the ferroelectric distortion, while strong JT distortion enables Mn^{3+} to effectively couple to the $BaTiO_3$ lattice. Also, the δ_{Mn} values are noticeably larger than the corresponding δ_{Nb} values for a given composition, revealing stronger distortion (JT-induced) about Mn ions compared to Nb (off-center displaced). This explains why the local environment about Mn exhibits higher disorder (σ^2) as compared to Nb. It is important to remember that even though some level of distortion persists locally for all x, doping systematically leads to reduction of tetragonality, eventually making the system cubic at $x = 0.1$. Ferroelectricity in $BaTiO_3$ is driven by long-range ordered displacement of Ti. Mn−Nb co-doping disrupts the Ti−O covalent bonding, limiting long-range polar ordering. The P value, therefore is determined by the balance between these long-range Coulombic forces and doping induced short-range interatomic forces. Beyond a critical doping threshold ($x \geq 0.1$), the macroscopic polarization eventually goes to 0 and the system becomes paraelectric.[28]

Figure 7 also highlights the anomalous behavior of the $x = 0.075$ sample, showing an increase of polarization (P) and distortion effects. We recall here that for the $x = 0.075$ sample the $\chi(R)$ functions for both Mn (Figure 3b) and Nb (Figure 5b) data reveal severe dampening effects, especially visible for the higher order peak (~3.2 Å). We also found maximum spread of σ^2 values associated with different sublattices (Figures 4b and 6b), with unusually high values for the Mn−M and Nb−M pairs. This typically happens as EXAFS cannot fully resolve multiple local structures closely resembling each other and therefore accounts for it by a single broad bond distribution. One common origin for such multiple environments is local chemical inhomogeneities at the B-site, for example, dopant clustering effects. In such a scenario, the dopant-rich small fraction of the sample would exhibit high disorder and low polarization, whereas the Ti-rich major fraction would essentially behave as a pure undisrupted $BaTiO_3$ lattice, eventually resulting in higher P values. Thus, one cannot rule out the possibility that $x = 0.075$ experiences dopant clustering effects. Such local effects, as often observed, remain intimately connected to the overall lattice, thereby affecting the bulk band gap. The structural peculiarity of $x = 0.075$ possibly stems from the fact that tetragonal to cubic phase transition point in BTMNO lies in the vicinity of $x = 0.075$. This region is hence sensitive since small composition changes can affect major structural changes. Still, however, the $x = 0.075$ sample was, in fact, fairly reproducible. A more accurate description of such unique structural anomalies requires detailed calculations. Nonetheless, Figure 7 implies that co-doping of Mn^{3+} and Nb^{5+} can induce strong electron−lattice coupling, which in turn is capable of sustaining the ferroelectric distortion prevalent in tetragonal BTMNO. This explains how the inherent $BaTiO_3$ polarization is preserved to a considerable extent even in the presence of a non-d^0 system like Mn^{3+}. Such coupling remains effective up to an optimal doping limit, beyond which the system would assume a higher symmetry cubic phase, as we see for $x = 0.1$.

CONCLUSIONS

We have studied how the local structural effects about B-sites (dopants: Mn and Nb; host: Ti) can influence material functionality in the room temperature low band gap ferroelectric system BTMNO, where Mn is primarily responsible for reducing the band gap and Nb acts as a charge compensator ion. Calculated Raman modes clearly identify Ti off-centering to be the driving force for such spontaneous polarization in the system. The intensity of the 1s → 3d quadrupolar transition, a measure of the extent of displacement of the B-site (Ti) from the O_6 octahedral center, correlates well with reported polarization values for a given composition. Our XAS studies reveal Mn^{3+} and Nb^{5+} to be the dominant charge states of the dopant species. Both dopants experience strong local structural distortions at the Ti sites, but the modes of distortion associated with the two dopants have fundamentally different origins. The Mn^{3+}−O_6 distortion could be related to the Jahn−Teller effect, while the Nb^{5+}−O_6 distortion could be associated with off-center displacement of Nb within the O_6 octahedra. A d^4 Mn^{3+} ion replacing Ti^{4+} helps to improve the photovoltaic functionality of $BaTiO_3$ through bulk band gap reduction and partial loss of polarization. However, the loss is significantly minimized by strong JT distortions about Mn^{3+} that adequately couple the Mn^{3+}−O_6 octahedra to the overall ferroelectric $BaTiO_3$ lattice. A d^0 Nb^{5+} ion replacing Ti^{4+}, in contrast, partially compensates for this small loss of polarization by replenishing the number of d^0 ions but barely participates in band gap tunability. The relatively stronger extent of distortion of Mn^{3+} within the O_6 octahedra introduces higher disorder in $BaTiO_3$ compared to Nb^{5+}. We find the Mn and Nb residing at Ti sites to be an effective charge neutral pair with insignificant charge disproportionation effects. Rather, the Mn^{3+}−Nb^{5+} pair has the ability to integrate with the tetragonal $BaTiO_3$ lattice, preserving the intrinsic polarization to a considerable extent. Our findings reveal how BTMNO material functionality can be correlated to complex B-site local distortions, thereby highlighting the effectiveness of controlled co-doping strategies in making promising ferroelectric photovoltaics and other optoelectronic applications in the future.

ASSOCIATED CONTENT

Supporting Information

The Supporting Information is available free of charge at https://pubs.acs.org/doi/10.1021/acs.jpcc.1c02539.

Ti K pre-edge fine structure fits, EXAFS data analyses, fits to Mn K and Nb K data for BTMNO in $\chi(k)$, real part of $\chi(R)$ and modulus of the $\chi(R)$ functions, Mn K and Nb K EXAFS parameters, simulations for distortion models within O6 octahedra, $\chi(k)$ functions for (a) Mn and (b) Nb in BTMNO systems (PDF)

AUTHOR INFORMATION

Corresponding Authors

Håkan Rensmo − *Department of Physics and Astronomy, Molecular and Condensed Matter Physics, Uppsala University, SE-75120 Uppsala, Sweden;* orcid.org/0000-0001-5949-0997; Email: hakan.rensmo@physics.uu.se

Soham Mukherjee − *Department of Physics and Astronomy, Molecular and Condensed Matter Physics, Uppsala University, SE-75120 Uppsala, Sweden;* Email: soham.mukherjee@physics.uu.se

Authors

Dibya Phuyal − *Division of Material and Nano Physics, Department of Applied Physics, KTH Royal Institute of Technology, 114 28 Stockholm, Sweden;* orcid.org/0000-0003-0351-3138

Carlo U. Segre − *CSRRI and Department of Physics, Illinois Institute of Technology, Chicago, Illinois 60616, United States;* orcid.org/0000-0001-7664-1574

Shyamashis Das − *Department of Chemistry, Ramananda College, Bishnupur 722122 West Bengal, India*

Olof Karis − *Department of Physics and Astronomy, Molecular and Condensed Matter Physics, Uppsala University, SE-75120 Uppsala, Sweden;* orcid.org/0000-0001-6406-217X

Tomas Edvinsson − *Department of Engineering Sciences − Solid State Physics, Uppsala University, 75121 Uppsala, Sweden;* orcid.org/0000-0003-2759-7356

Complete contact information is available at: https://pubs.acs.org/10.1021/acs.jpcc.1c02539

Notes

The authors declare no competing financial interest.

■ ACKNOWLEDGMENTS

The authors especially want to thank Prof. DD Sarma for very inspirational collaboration over the years and for introducing us into the research area. We thank STandUP for Energy, the Swedish Research Council (Grants VR 2018-06465, 2018-04330, and 2019-05591), the Swedish Foundation for Strategic Research (Project RMA15-0130), and the Swedish Energy Agency (Grants P43549-1, P50626-1) for financial support. D.P. acknowledges the Swedish Research Council (Grant 2020-00681). T.E. acknowledges use of computational resources provided by the Swedish National Infrastructure for Computing (SNIC) under Projects snic2019-3-542 and snic2019-3-461. We thank DST CSIR, NSF, and DFG for funding this investigation. MRCAT operations are supported by the Department of Energy and the MRCAT member institutions. This research used resources of the Advanced Photon Source, a U.S. Department of Energy (DOE) Office of Science User Facility operated for the DOE Office of Science by Argonne National Laboratory under Contract DE-AC02-06CH11357. Support for C.U.S. was provided in part by the National Science Foundation under Grant DMR-086935.

■ ABBREVIATIONS

BTMNO, $BaTi_{1-x}(Mn_{0.5}Nb_{0.5})_xO_3$; XAS, X-ray absorption spectroscopy; XANES, X-ray absorption near-edge structure; EXAFS, extended X-ray absorption fine structure; JT, Jahn−Teller; JT-(*o*), Jahn−Teller (orthorhombic); JT-(*t*), Jahn−Teller (tetragonal); OC, off-centering; CD, charge disproportionation; MS, multiple sites.

■ REFERENCES

(1) von Hippel, A.; Breckenridge, R. G.; Chesley, F. G.; Tisza, L. High Dielectric Constant Ceramics. *Ind. Eng. Chem.* **1946**, *38* (11), 1097−1109.

(2) Scott, J. F. Applications of Modern Ferroelectrics. *Science (Washington, DC, U. S.)* **2007**, *315* (5814), 954−960.

(3) Dawber, M.; Rabe, K. M.; Scott, J. F. Physics of Thin-Film Ferroelectric Oxides. *Rev. Mod. Phys.* **2005**, *77* (4), 1083−1130.

(4) Hennings, D.; Klee, M.; Waser, R. Advanced Dielectrics: Bulk Ceramics and Thin Films. *Adv. Mater.* **1991**, *3* (7), 334−340.

(5) Wang, S.-F.; Dayton, G. O. Dielectric Properties of Fine-Grained Barium Titanate Based X7R Materials. *J. Am. Ceram. Soc.* **1999**, *82* (10), 2677−2682.

(6) Bhattacharya, K.; Ravichandran, G. Ferroelectric Perovskites for Electromechanical Actuation. *Acta Mater.* **2003**, *51*, 5941−5960.

(7) Su, L.; Zou, L.; Fong, C.-C.; Wong, W.-L.; Wei, F.; Wong, K.-Y.; Wu, R. S. S.; Yang, M. Detection of Cancer Biomarkers by Piezoelectric Biosensor Using PZT Ceramic Resonator as the Transducer. *Biosens. Bioelectron.* **2013**, *46*, 155−161.

(8) Damjanovic, D.; Muralt, P.; Setter, N. Ferroelectric Sensors. *IEEE Sens. J.* **2001**, *1* (3), 191−206.

(9) Tang, P.; Towner, D. J.; Meier, A. L.; Wessels, B. W. Low-Loss Electrooptic $BaTiO_3$ Thin Film Waveguide Modulator. *IEEE Photonics Technol. Lett.* **2004**, *16* (8), 1837−1839.

(10) Petraru, A.; Schubert, J.; Schmid, M.; Buchal, Ch Ferroelectric $BaTiO_3$ Thin-Film Optical Waveguide Modulators. *Appl. Phys. Lett.* **2002**, *81* (8), 1375−1377.

(11) Scott, J. F.; Paz De Araujo, C. A. Ferroelectric Memories. *Science (Washington, DC, U. S.)* **1989**, *246* (4936), 1400−1405.

(12) Spanier, J. E.; Fridkin, V. M.; Rappe, A. M.; Akbashev, A. R.; Polemi, A.; Qi, Y.; Gu, Z.; Young, S. M.; Hawley, J.; Imbrenda, D.; et al. Power Conversion Efficiency Exceeding the Shockley-Queisser Limit in a Ferroelectric Insulator. *Nat. Photonics* **2016**, *10*, 611−616.

(13) Huang, H. Ferroelectric Photovoltaics. *Nat. Photonics* **2010**, *4* (3), 134−135.

(14) Hu, Y.; Florio, F.; Chen, Z.; Phelan, W. A.; Siegler, M. A.; Zhou, Z.; Guo, Y.; Hawks, R.; Jiang, J.; Feng, J.; et al. A Chiral Switchable Photovoltaic Ferroelectric 1D Perovskite. *Sci. Adv.* **2020**, *6* (9), 1−10.

(15) You, L.; Zheng, F.; Fang, L.; Zhou, Y.; Tan, L. Z.; Zhang, Z.; Ma, G.; Schmidt, D.; Rusydi, A.; Wang, L.; Chang, L.; Rappe, A. M.; Wang, J. Enhancing Ferroelectric Photovoltaic Effect by Polar Order Engineering. *Sci. Adv.* **2018**, *4* (7), 1−10.

(16) Grinberg, I.; West, D. V.; Torres, M.; Gou, G.; Stein, D. M.; Wu, L.; Chen, G.; Gallo, E. M.; Akbashev, A. R.; Davies, P. K.; et al. Perovskite Oxides for Visible-Light-Absorbing Ferroelectric and Photovoltaic Materials. *Nature* **2013**, *503* (7477), 509−512.

(17) Paillard, C.; Bai, X.; Infante, I. C.; Guennou, M.; Geneste, G.; Alexe, M.; Kreisel, J.; Dkhil, B. Photovoltaics with Ferroelectrics: Current Status and Beyond. *Adv. Mater.* **2016**, *28*, 5153−5168.

(18) Cohen, R. E. Origin of Ferroelectricity in Perovskite Oxides. *Nature* **1992**, *358*, 136−138.

(19) Krawczyk, P. A.; Jurczyszyn, M.; Pawlak, J.; Salamon, W.; Baran, P.; Kmita, A.; Gondek, L.; Sikora, M.; Kapusta, C.; Strączek, T.; et al. High-Entropy Perovskites as Multifunctional Metal Oxide Semiconductors_ Synthesis and Characterization of $(Gd_{0.2}Nd_{0.2}La_{0.2}Sm_{0.2}Y_{0.2})CoO_3$. *ACS Appl. Electron. Mater.* **2020**, *2*, 3211−3220.

(20) Wang, Y.; Wang, C.; Liang, W.; Song, X.; Zhang, Y.; Huang, M.; Jiang, H. Multifunctional Perovskite Oxide for Efficient Solar-Driven Evaporation and Energy-Saving Regeneration. *Nano Energy* **2020**, *70*, 104538.

(21) Jana, S.; Panda, S. K.; Phuyal, D.; Pal, B.; Mukherjee, S.; Dutta, A.; Kumar, P. A.; Hedlund, D.; Schött, J.; Thunström, P.; et al. Charge Disproportionate Antiferromagnetism at the Verge of the Insulator-Metal Transition in Doped $LaFeO_3$. *Phys. Rev. B: Condens. Matter Mater. Phys.* **2019**, *99* (7), 075106.

(22) Phuyal, D.; Mukherjee, S.; Panda, S. K.; Jana, S.; Segre, C. U.; Simonelli, L.; Butorin, S. M.; Rensmo, H.; Karis, O. Origin of Itinerant Carriers in Antiferromagnetic $LaFe_{1-x}Mo_xO_3$ Studied by X-Ray Spectroscopies. *Phys. Rev. Mater.* **2020**, *4* (3), 034405.

(23) Yuan, Y.; Xiao, Z.; Yang, B.; Huang, J. Arising Applications of Ferroelectric Materials in Photovoltaic Devices. *J. Mater. Chem. A* **2014**, *2*, 6027−6041.

(24) Nechache, R.; Harnagea, C.; Li, S.; Cardenas, L.; Huang, W.; Chakrabartty, J.; Rosei, F. Bandgap Tuning of Multiferroic Oxide Solar Cells. *Nat. Photonics* **2015**, *9*, 61−67.

(25) Hill, N. A. Why Are There so Few Magnetic Ferroelectrics? *J. Phys. Chem. B* **2000**, *104* (29), 6694−6709.

(26) Wang, S.-F.; Wu, Y.-C.; Hsu, Y.-C.; Chu, J.-P.; Wu, C.-H. Properties of Hexagonal $Ba(Ti_{1-x}Mn_x)O_3$ Ceramics: Effects of Sintering Temperature and Mn Content. *Jpn. J. Appl. Phys.* **2007**, *46* (5A), 2978−2983.
(27) Benedek, N. A.; Fennie, C. J. Why Are There So Few Perovskite Ferroelectrics? *J. Phys. Chem. C* **2013**, *117*, 13339−13349.
(28) Das, S.; Ghara, S.; Mahadevan, P.; Sundaresan, A.; Gopalakrishnan, J.; Sarma, D. D. Designing a Lower Bandgap Bulk Ferroelectric Material with a Sizable Polarization at the Room Temperature. *ACS Energy Lett.* **2018**, *3*, 1176−1182.
(29) Phuyal, D.; Mukherjee, S.; Das, S.; Jana, S.; Kvashnina, K. O.; Sarma, D. D.; Rensmo, H.; Buortin, S. M.; Karis, O. The Origin of Low Bandgap and Ferroelectricity of a co-doped $BaTiO_3$. *EPL (Europhysics Letters)* **2018**, *124* (2), 27005.
(30) Frenkel, A. I.; Wang, F. M.; Kelly, S.; Ingalls, R.; Haskel, D.; Stern, E. A.; Yacoby, Y. Local Structural Changes in $KNbO_3$ under High Pressure. *Phys. Rev. B: Condens. Matter Mater. Phys.* **1997**, *56* (17), 10869−10877.
(31) Lemeshko, M. P.; Nazarenko, E. S.; Gonchar, A. A.; Reznichenko, L. A.; Nedoseykina, T. I.; Novakovich, A. A.; Mathon, O.; Joly, Y.; Vedrinskii, R. V. EXAFS Studies of the Local Atomic Structure of the Lead-Free Piezoelectric Ceramics $K_xNa_{1-x}NbO_3$ over the Temperature Range 10 - 1023 K. *Phys. Rev. B: Condens. Matter Mater. Phys.* **2007**, *76*, 134106.
(32) Ivliev, M. P.; Raevskaya, S. I.; Raevskii, I. P.; Shuvaeva, V. A.; Pirog, I. V. Formation of Ferroelectric Phases in $KNbO_3$ and Other Niobates with Perovskite Structure. *Phys. Solid State* **2007**, *49* (4), 769−779.
(33) Phuyal, D.; Mukherjee, S.; Jana, S.; Denoel, F.; Kamalakar, M. V.; Butorin, S. M.; Kalaboukhov, A.; Rensmo, H.; Karis, O. Ferroelectric Properties of $BaTiO_3$ Thin Films co-doped with Mn and Nb. *AIP Adv.* **2019**, *9* (9), 095207.
(34) Kola, L.; Murali, D.; Pal, S.; Nanda, B. R. K.; Murugavel, P. Enhanced Bulk Photovoltaic Response in Sn Doped $BaTiO_3$ through Composition Dependent Structural Transformation. *Appl. Phys. Lett.* **2019**, *114* (18), 183901.
(35) Pal, S.; Muthukrishnan, S.; Sadhukhan, B.; Sarath, N. V.; Murali, D.; Murugavel, P. Bulk Photovoltaic Effect in $BaTiO_3$-based Ferroelectric Oxides: An Experimental and Theoretical Study. *J. Appl. Phys.* **2021**, *129* (084106), 1−9.
(36) Balzarotti, A.; Czyżyk, M.; Kisiel, A.; Motta, N.; Podgòrny, M.; Zimnal-Starnawska, M. Local Structure of Ternary Semiconducting Random Solid Solutions: Extended x-Ray-Absorption Fine Structure of $Cd_{1-x}Mn_xTe$. *Phys. Rev. B: Condens. Matter Mater. Phys.* **1984**, *30* (4), 2295−2298.
(37) Mukherjee, S.; Nag, A.; Kocevski, V.; Santra, P. K.; Balasubramanian, M.; Chattopadhyay, S.; Shibata, T.; Schaefers, F.; Rusz, J.; Gerard, C.; et al. Microscopic Description of the Evolution of the Local Structure and an Evaluation of the Chemical Pressure Concept in a Solid Solution. *Phys. Rev. B: Condens. Matter Mater. Phys.* **2014**, *89* (22), 224105.
(38) Pradhan, J.; Mukherjee, S.; Khan, A. H.; Dalui, A.; Satpati, B.; Segre, C. U.; Sarma, D. D.; Acharya, S. Two-Dimensional Hybrid Organohalide Perovskites from Ultrathin PbS Nanocrystals as Template. *J. Phys. Chem. C* **2017**, *121*, 6401−6408.
(39) Khan, A. H.; Dalui, A.; Mukherjee, S.; Segre, C. U.; Sarma, D. D.; Acharya, S. Efficient Solid-State Light-Emitting CuCdS Nanocrystals Synthesized in Air. *Angew. Chem., Int. Ed.* **2015**, *54* (9), 2643−2648.
(40) Ravel, B.; Newville, M. ATHENA, ARTEMIS, HEPHAESTUS: Data Analysis for X-Ray Absorption Spectroscopy Using IFEFFIT. *J. Synchrotron Radiat.* **2005**, *12*, 537−541.
(41) Zabinsky, S. I.; Rehr, J. J.; Ankudinov, A.; Albers, R. C.; Eller, M. J. Multiple-Scattering Calculations of x-Ray-Absorption Spectra. *Phys. Rev. B: Condens. Matter Mater. Phys.* **1995**, *52* (4), 2995−3009.
(42) Dovesi, R.; Saunders, V. R.; Roetti, C.; Orlando, R.; Zicovich-Wilson, C. M.; Pascale, F.; Civalleri, B.; Doll, K.; Harrison, N. M.; Bush, I. J.; et al. *CRYSTAL17 User's Manual*; University of Torino: Torino, 2017.
(43) Dovesi, R.; Erba, A.; Orlando, R.; Zicovich-Wilson, C. M.; Civalleri, B.; Maschio, L.; Rerat, M.; Casassa, S.; Baima, J.; Salustro, S.; Kirtman, B. Quantum-Mechanical Condensed Matter Simulations with CRYSTAL. *Wiley Interdiscip. Rev.: Comput. Mol. Sci.* **2018**, *8*, No. e1360.
(44) Peintinger, M. F.; Oliveira, D. V.; Bredow, T. Consistent Gaussian Basis Sets of Triple-Zeta Valence with Polarization Quality for Solid-State Calculations. *J. Comput. Chem.* **2013**, *34*, 451−459.
(45) Hay, P. J.; Wadt, W. R. *Ab initio* Effective Core Potentials for Molecular Calculations. Potentials for the Transition Metal Atoms Sc to Hg. *J. Chem. Phys.* **1985**, *82* (1), 270−283.
(46) Piskunov, S.; Heifets, E.; Eglitis, R. I.; Borstel, G. Bulk Properties and Electronic Structure of $SrTiO_3$, $BaTiO_3$, $PbTiO_3$ Perovskites: An *ab initio* HF/DFT Study. *Comput. Mater. Sci.* **2004**, *29*, 165−178.
(47) Monkhorst, H. J.; Pack, J. D. Special Points for Brillonin-Zone Integrations. *Phys. Rev. B* **1976**, *13* (12), 5188−5192.
(48) Maschio, L.; Kirtman, B.; Rérat, M.; Orlando, R.; Dovesi, R. *Ab Initio* Analytical Raman Intensities for Periodic Systems through a Coupled Perturbed Hartree-Fock/Kohn-Sham Method in an Atomic Orbital Basis. II. Validation and Comparison with Experiments. *J. Chem. Phys.* **2013**, *139*, 164101.
(49) Bilc, D. I.; Orlando, R.; Shaltaf, R.; Rignanese, G.-M.; Íñiguez, J.; Ghosez, Ph Hybrid Exchange-Correlation Functional for Accurate Prediction of the Electronic and Structural Properties of Ferroelectric Oxides. *Phys. Rev. B: Condens. Matter Mater. Phys.* **2008**, *77* (16), 165107.
(50) Freire, J. D.; Katiyar, R. S. Lattice Dynamics of Crystals with Tetragonal $BaTiO_3$ Structure. *Phys. Rev. B: Condens. Matter Mater. Phys.* **1988**, *37* (4), 2074−2085.
(51) Pokorńy, J.; Pasha, U. M.; Ben, L.; Thakur, O. P.; Sinclair, D. C.; Reaney, I. M. Use of Raman Spectroscopy to Determine the Site Occupancy of Dopants in $BaTiO_3$. *J. Appl. Phys.* **2011**, *109* (11), 114110.
(52) Yamamoto, T.; Mizoguchi, T.; Tanaka, I. Core-Hole Effect on Dipolar and Quadrupolar Transitions of $SrTiO_3$ and $BaTiO_3$ at Ti K Edge. *Phys. Rev. B: Condens. Matter Mater. Phys.* **2005**, *71* (24), 245113.
(53) Vedrinskii, R. V.; Kraizman, V. L.; Novakovich, A. A.; Demekhin, P. V.; Urazhdin, S. V. Pre-Edge Fine Structure of the 3d Atom K x-Ray Absorption Spectra and Quantitative Atomic Structure Determinations for Ferroelectric Perovskite Structure Crystals. *J. Phys.: Condens. Matter* **1998**, *10* (42), 9561−9580.
(54) Booth, C. H.; Bridges, F.; Kwei, G. H.; Lawrence, J. M.; Cornelius, A. L.; Neumeier, J. J. Lattice Effects in $La_{1-x}Ca_xMnO_3$ (x = 001): Relationships between Distortions, Charge Distribution, and Magnetism. *Phys. Rev. B: Condens. Matter Mater. Phys.* **1998**, *57* (17), 10440−10454.
(55) Tan, T.-Y.; Kennedy, B. J.; Zhou, Q.; Ling, C. D.; Miiller, W.; Howard, C. J.; Carpenter, M. A.; Knight, K. S. Impact of Jahn-Teller Active Mn^{3+} on Strain Effects and Phase Transitions in $Sr_{0.65}Pr_{0.35}MnO_3$. *Phys. Rev. B: Condens. Matter Mater. Phys.* **2012**, *85* (10), 104107.
(56) Lebedev, A. I.; Sluchinskaya, I. A.; Erko, A.; Kozlovskii, V. F. Direct Evidence for Off-Centering of Mn Impurity in $SrTiO_3$. *JETP Lett.* **2009**, *89* (9), 457−460.
(57) Shannon, R. D. Revised Effective Ionic Radii and Systematic Studies of Interatomie Distances in Halides and Chaleogenides. *Acta Crystallogr., Sect. A: Cryst. Phys., Diffr., Theor. Gen. Crystallogr.* **1976**, *A32*, 751−767.
(58) Mukherjee, S.; Ganegoda, H.; Kumar, A.; Pal, S.; Segre, C. U.; Sarma, D. D. Evolution of the Local Structure within Chromophoric Mn-O5 Trigonal Bipyramids in $YMn_{1-x}In_xO_3$ with Composition. *Inorg. Chem.* **2018**, *57* (15), 9012−9019.
(59) Hocking, R. K.; Brimblecombe, R.; Chang, L. Y.; Singh, A.; Cheah, M. H.; Glover, C.; Casey, W. H.; Spiccia, L. Water-Oxidation Catalysis by Manganese in a Geochemical-like Cycle. *Nat. Chem.* **2011**, *3* (6), 461−466.

https://doi.org/10.1021/acs.jpcc.1c02539
J. Phys. Chem. C 2021, 125, 14910−14923

(60) Cartier, C.; Hammouda, T.; Boyet, M.; Mathon, O.; Testemale, D.; Moine, B. N. Evidence for Nb^{2+} and Ta^{3+} in Silicate Melts under Highly Reducing Conditions: A XANES Study. *Am. Mineral.* **2015**, *100*, 2152−2158.
(61) Shuvaeva, V. A.; Pirog, I.; Azuma, Y.; Yagi, K.; Sakaue, K.; Terauchi, H.; Raevskii, I. P.; Zhuchkov, K.; Antipin, M. Yu. The Local Structure of Mixed-Ion Perovskites. *J. Phys.: Condens. Matter* **2003**, *15*, 2413−2421.
(62) Vedrinskii, R. V.; Kraizman, V. L.; Lemeshko, M. P.; Nazarenko, E. S.; Novakovich, A. A.; Reznichenko, L. A.; Fokin, V. N.; Shuvaeva, V. A. Local Atomic Structure of Niobates and Titanates from X-Ray Absorption Spectroscopic Data. *Phys. Solid State* **2009**, *51* (7), 1394−1398.
(63) Bugaev, L. A.; Shuvaeva, V. A.; Alekseenko, I. B.; Zhuchkov, K. N.; Vedrinskii, R. V. Determination of the Local Structure of NbO_6 Octahedra in the Orthorhombic Phase of a $KNbO_3$ Crystal Using EXAFS. *Phys. Solid State* **1998**, *40* (6), 1001−1005.
(64) Masó, N.; Beltrán, H.; Cordoncillo, E.; Flores, A. A.; Escribano, P.; Sinclair, D. C.; West, A. R. Synthesis and Electrical Properties of Nb-doped $BaTiO_3$. *J. Mater. Chem.* **2006**, *16*, 3114−3119.
(65) Kowalski, K.; Ijjaali, M.; Bak, T.; Dupre, B.; Nowotny, J.; Rekas, M.; Sorrell, C. C. Electrical Properties of Nb-doped $BaTiO_3$. *J. Phys. Chem. Solids* **2001**, *62*, 543−551.

https://doi.org/10.1021/acs.jpcc.1c02539
J. Phys. Chem. C 2021, 125, 14910−14923